Energy 282 (2023) 128800

Contents lists available at ScienceDirect

Energy

journal homepage: www.elsevier.com/locate/energy

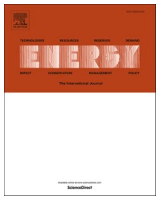

Experimental and simulation study of Mn–Fe particles in a controllable-flow particle solar receiver for high-temperature thermochemical energy storage

Di Gan [a,b], Peiwang Zhu [a,b,c,**], Haoran Xu [a,b,c], Xiangyu Xie [a,b], Fengyuan Chai [a,b], Jueyuan Gong [a,b], Jiasong Li [a,b], Gang Xiao [a,b,c,*]

[a] Key Laboratory of Clean Energy and Carbon Neutrality of Zhejiang Province, Zhejiang University, 38 Zheda Road, Hangzhou, Zhejiang, 310027, China
[b] State Key Laboratory of Clean Energy Utilization, Zhejiang University, 38 Zheda Road, Hangzhou, 310027, China
[c] Jiaxing Research Institute, Zhejiang University, 1300 Dongshengxilu Road, Jiaxing, 314031, China

ARTICLE INFO

Handling editor: Soteris Kalogirou

Keywords:
Thermochemical energy storage
Controllable-flow particle receiver
Mn–Fe particles
Experiment
Receiver model

ABSTRACT

CSP systems hold tremendous potential for large-scale and long-duration energy storage. However, their extensive adoption has been impeded by cost constraints. To overcome this hurdle, the development of the next generation CSP systems, focusing on high-temperature heat absorption and storage, is paramount for reducing the LCOE. The integration of TCES technologies shows promise in bolstering energy storage density, stability at high temperatures, and decreasing the LCOE. This study investigates the performance of Mn–Fe particles in a controllable-flow particle receiver operating at high temperatures. Experimental data demonstrate that the particles reach a maximum temperature of 1041.8 °C, resulting in an outstanding outlet particle thermochemical reaction conversion rate of 96.35%. Critical parameters influencing receiver performance were also examined meticulously. It was observed that increased incident flux density significantly enhanced receiver efficiency of 88%. Moreover, effective management of local overheating through the integration of TCES proved indispensable. The outlet particle temperature differential was merely 9.53 °C, and the sudden fluctuations in incident flux led to a limited temperature rise of 4.84 °C, attributing to intensified reaction enthalpy and reaction rate. By optimizing operational stability, continuous operation of CSP systems under high temperatures can be achieved, maximizing efficiency and allowing for greater system flexibility.

1. Introduction

In the wake of the escalating global environmental crisis, the proportion of renewable energy is continually surging, accompanied by an increasing demand for large-scale energy storage [1–3]. Thermochemical energy storage boasts remarkable advantages, including high energy storage density, wide reaction temperature range, and long-term heat retention capabilities, distinguishing it from other thermal energy storage systems, thereby rendering it a promising means for large-scale energy storage [4–7]. Redox systems represent one of the main types of thermochemical energy storage that enable heat storage and release reactions in an air atmosphere with oxygen as the reactant gas. They can be used in an open system without necessitating special requirements for air tightness, underscoring their potential in the field of thermochemical heat storage. Among metal oxide couples in redox systems [8–10], manganese oxides possess abundant reserves, non-toxicity, and inexpensive nature, rendering it highly feasible and possessing significant development potential [10–13]. Recent studies have explored various strategies to enhance the redox performance of manganese oxides [14,15]. These strategies include doping manganese oxide with Fe_2O_3, as demonstrated by Wong et al. [10] and Agrafiotis [16] et al., who reported enhanced redox performance. Al-Shankiti et al. [17] found that spray-dried Fe67 particles showed the best activity among tested materials, while Xiang et al. [12] and Carrillo [15,18] et al. gained

* Corresponding author. Key Laboratory of Clean Energy and Carbon Neutrality of Zhejiang Province, Zhejiang University, 38 Zheda Road, Hangzhou, Zhejiang, 310027, China.
** Corresponding author. Key Laboratory of Clean Energy and Carbon Neutrality of Zhejiang Province, Zhejiang University, 38 Zheda Road, Hangzhou, Zhejiang, 310027, China.
E-mail addresses: zhupw@zju.edu.cn (P. Zhu), xiaogangtianmen@zju.edu.cn (G. Xiao).

https://doi.org/10.1016/j.energy.2023.128800
Received 21 March 2023; Received in revised form 21 July 2023; Accepted 16 August 2023
Available online 17 August 2023

fundamental insights into Mn–Fe materials' redox mechanism. Overall, iron-manganese particles' faster redox reaction rate enables rapid heat storage and release, making it suitable for multiple high-temperature applications [19].

CSP technology possesses immense potential for large-scale and long-duration energy storage, effectively mitigating the intermittent of solar energy. As of 2021, the LCOE for CSP stands at $0.114/kWh, leaving room for further reduction [20]. Undoubtedly, there exists a compelling pathway towards achieving lower LCOE through the introduction of next-generation CSP technologies, notably the integration of high-temperature heat absorption and storage with supercritical CO_2 Brayton cycles. This ground-breaking enhancement aims to optimize the conversion efficiency of solar energy to electricity, thereby facilitating substantial cost reduction. Furthermore, a key avenue for enhancing the economic viability of CSP systems lies in elevating the energy storage density of materials, enabling reductions in both land occupation and equipment expenditures [21]. The reduction reaction temperature of manganese iron oxide is well suited for the high operating temperatures (>1000 °C) required by particle solar power tower systems [11,22]. Meanwhile, the oxidation reaction temperature range can provide a viable heat source for supercritical carbon dioxide Brayton cycle, enhancing the thermal efficiency of high-temperature thermal power generation systems and reducing electricity costs further [23–25]. Numerous scholars have conducted research on the heat storage and release process of thermochemical materials [26]. Based on a packed bed tube reactor, systematic investigation and parametric studies using $(Mn_{0.75}Fe_{0.25})_2O_3$ particles concluded that heat capacity rates were the most important factor for the storage process by Woken et al. [27]. Preisner et al. investigated a counter-current moving bed with manganese-iron-oxide using a 1D transient model. The combination of sensible energy and thermochemical energy from $(Mn_{0.75}Fe_{0.25})_2O_3$ particles reached 933 kJ/kg when cooling from 1050 °C to 300 °C [28]. Moreover, Hamdi et al. heated the Fe67 particle inside a packed bed reactor with an electric IR furnace and developed a 2D model transient model to analyze the reduction process [29]. Wang et al. developed a transient heat transfer model of an indirectly irradiated tubular fluidized bed reactor to reduce manganese oxide particles, estimating solar-to-thermochemical efficiency between 46.3% and 57.4% [13,30]. Wang et al. also developed a comprehensive transient 3D model to obtain packed Fe67 particle reduction performance in the thermochemical reactor, validated by experimental data [31]. Stefania et al. proposed a thermochemical storage system consisting of a rotary kiln and a moving bed utilizing Mn–Fe oxide particles as storage material. Among 14 cycles, the outlet particle temperature reached nearly 1000 °C, and the maximum conversion rate was about 70% [32]. Furthermore, other metal oxides have also been studied and could provide valuable insights. Andrew et al. tested a 5 kW_{th} granular-flow reactor, resulting in temperatures over 1073 K and absorption efficiency of 64.7% [33]. Zhou et al. developed a 1D model of ceramics honeycomb coated with cobalt oxides, presenting the storage vessel temperature of different positions [34]. Wei et al. presented a 1D model of reduction reaction. The thermal-to-chemical efficiency and system efficiency were about 95% and 30%, respectively [35]. Based on this [35], David et al. developed a 2D axisymmetric model for packed-bed and counter-flow moving-bed reactors with $(Mn_{0.75}Fe_{0.25})_2O_3$ and $(Mg_xMnO_{1+x\ +\ y1})$, respectively [36]. Based on the aforementioned studies, it is evident that there is currently a lack of experimental and simulation research on continuous heat absorption of particles under concentrated flux. Further analysis is necessary to understand the influence of key parameters of thermochemical reactions on the heat absorption processes of the particles. Moreover, in the experimental test of continuous heat absorption of particles under concentrated flux, there is still room for improvement in the particle thermochemical reaction conversion rate (~70%). Enhancing this conversion rate is crucial to fully exploit the high energy storage density advantages offered by TCES.

Solar particle receivers are an essential component of CSP systems, as they enable the conversion of fluctuating solar energy into stable thermal energy for storage [37–40]. Various types of solar particle receivers exist, including free-falling [41–43], rotary kiln [44,45], fluidized bed [22,46,47], quartz tube gravity-driven [23,48], and controllable-flow particle solar receivers [49,50]. Given the high temperatures required for the reaction and the need for both flow rate and heating time control, controllable-flow particle solar receivers appear to match well with the heat absorption process of high-temperature thermochemical particles. By controlling the residence time of particles, controllable-flow particle solar receivers offer an efficient means of managing heat transfer while maintaining high efficiency. This control ensures high reaction rates and enhances the conversion of solar energy into thermochemical energy. Storing solar energy in the form of thermochemical energy, rather than sensible heat, promotes a uniform distribution of particle temperatures on the heat-absorbing surface, minimizing thermal stresses on receiver equipment operating at high temperatures. This improves the long-term reliability of particle solar receivers for continuous operation. Integrating controllable-flow particle receivers presents significant opportunities for advancing CSP systems, optimizing their performance, and meeting the increasing demands of thermal energy storage.

To address the aforementioned issues and realize continuous heat absorption with high reaction conversion rates under concentrated solar irradiation, thermochemical energy storage coupled with controllable-flow particles receiver is a promising solution. Understanding the role of thermochemical energy storage in the heat absorption process is essential. In this study, we conducted experimental and simulation research on the continuous operation of heat absorption processes using Mn–Fe particles. A controllable-flow particle solar receiver testing system was developed for this purpose. The system enabled to experimentally investigate the receiver characteristics and reaction process of Mn–Fe particles, achieving high-temperature operation with high reaction conversion rates. This study integrated a reaction kinetics model for $(Mn_{0.8}Fe_{0.2})_2O_3$ particles with calculations of radiation, convection, heat conduction, and reaction heat. This integration allowed us to construct a transient model of the controllable-flow particle solar receiver. The model was validated with experimental data, and further analysis was conducted to explore the effects of incident flux density, reaction enthalpy, and reaction rate on the heat absorption process based on the receiver model. It was indicated that spontaneous thermochemical reactions can rapidly absorb substantial amounts of energy. This practical solution addresses the issue of overheating caused by sudden increases in flux density, while also providing sufficient buffering time for flow rate regulation. By coupling thermochemical energy storage, the adaptability of particle heat absorption to fluctuating concentrated solar irradiation can be improved, thereby enhancing its long-term operational reliability. This research contributes to the advancement of next-generation CSP and TCES technologies.

2. Experimental system

2.1. Material characteristics

In this study, $(Mn_{0.8}Fe_{0.2})_2O_3$ materials were used due to their superior redox performance [12,51]. Mn–Fe particles were synthesized through a high-temperature solid-state reaction method [52], and their critical physical and chemical properties were rigorously evaluated. These evaluations encompassed key parameters such as absorptivity, emissivity, bulk density, specific heat capacity, diameter, and reaction enthalpy. The heat transfer process-related properties of the $(Mn_{0.8}Fe_{0.2})_2O_3$ particles were summarized in Table 1.

2.2. Particle receiver experimental system

To meet the practical experimental requirements, the system (see Fig. 1) was divided into three parts: (a) a flux density distribution

Table 1
Heat transfer process relevant properties of $(Mn_{0.8}Fe_{0.2})_2O_3$ particles.

Property	Value	Unit	Source
Absorptivity	0.94	–	measured by RF-5000 Visible-infrared reflection measurement system.
Emissivity	0.81	–	measured by IR-2 dual-band emissivity measuring equipment.
Thermal conductivity	0.26	W/(m·k)	measured by TPS 2500S thermal conductivity meter.
Bulk density	1700	kg/m^3	Measured.
Specific heat capacity	$112.1 * T^{0.2992}$ (273 *K to* 950 *K*) $19.5 * T^{0.4804} + 334$ (950 *K to* 1812 *K*)	J/(kg·K)	Calculated and curve fitted based on Fe_2O_3 and Mn_3O_4 Specific heat capacity [12].
Particle average diameter	0.7	mm	Measured by Mastersizer 3000E particle size analyzer
Reaction enthalpy	171.95	kJ/kg	Measured by STARe System TGA/DSC 3+ [12].

measurement setup was employed to emit stable concentrated flux and measure the flux distribution on the particle receiver. (b) A controllable-flow solar particle receiver was used to absorb the concentrated flux and regulate the particle heating process. And (c) a reaction conversion rate test setup was utilized to collect the reduced particles and measure the reduction reaction rate. The subsequent sections provide a detailed explanation of each of these three parts.

2.2.1. *Controllable-flow solar particle receiver*

The controllable-flow solar particle receiver is where the particles undergo heat absorption and reduction reactions (see Fig. 2). The particles flow from the particle bin onto the heat-absorbing slope, gradually heating up as they advance, with the thickness of the particle layer increasing along the flow direction. A certain height of baffle structure is set at the outlet to allow high-temperature flowing particles in the surface layer to exit while retaining lower-temperature stagnant-layer particles within the particle receiver. The residence time of particles can be regulated by a gate valve connected to the funnel, which can match different incident flux densities to achieve the desired outlet temperature. Three thermocouples (p1, p2, p3) were placed at positions 10 cm, 2 cm from the particle outlet, and the outlet, respectively, with Agilent collecting real-time temperature data to study the heating characteristics of thermochemical particles and verify the receiver model in subsequent experiments.

2.2.2. *Reaction conversion rate test setup*

Real-time monitoring of the overall reaction in the particle receiver can be achieved by measuring oxygen concentration, allowing for

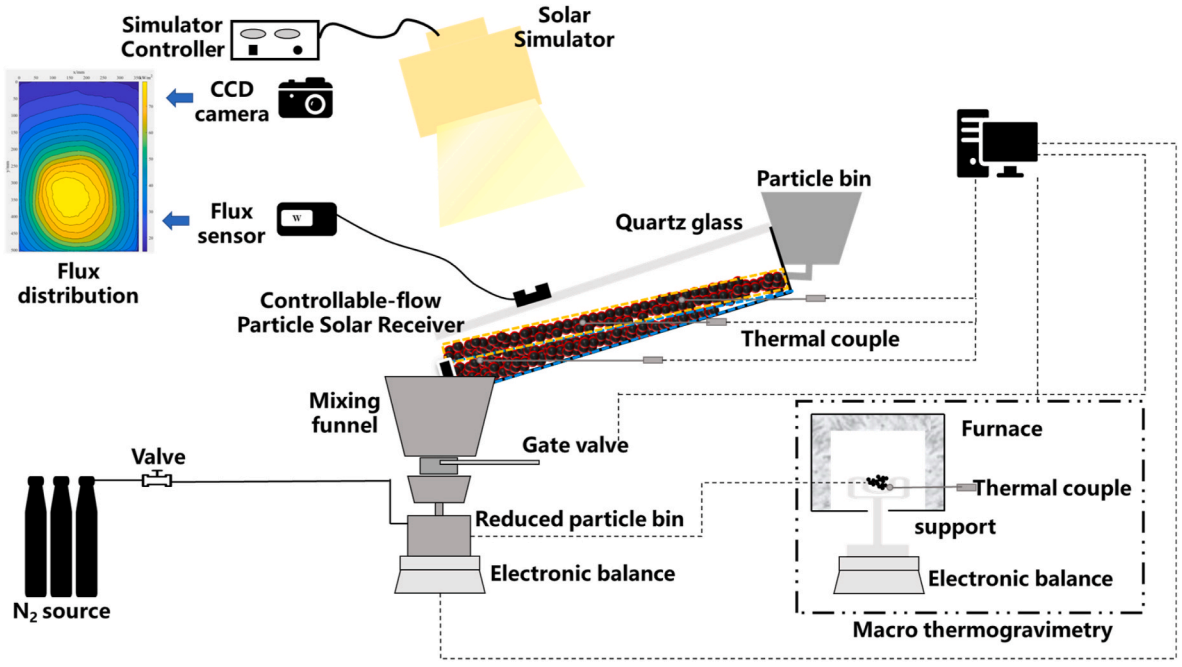

Fig. 1. Schematic diagram of particle receiver experimental system.

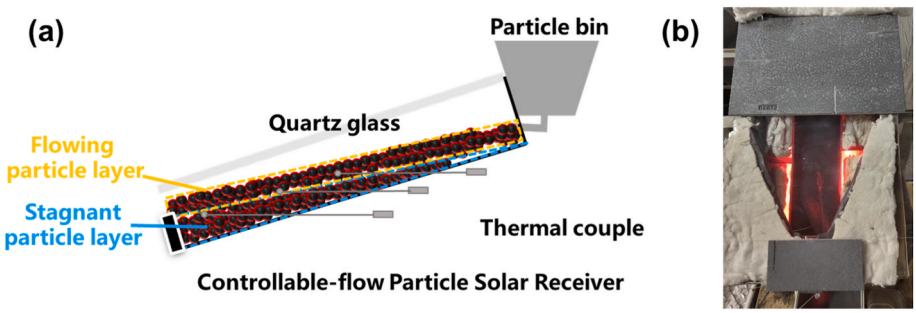

Fig. 2. (a) Schematic diagram of controllable-flow solar particle receiver. (b) Picture of controllable-flow solar particle receiver.

calculation of the overall conversion rate. However, this method faces challenges in continuously monitoring the conversion rate of thermochemical particles at the outlet under fluctuating incident flux conditions. To address this issue, a monitoring system based on the reduction rate of reaction products was designed to provide a key indicator monitoring method for regulating the particle receiver under realistic fluctuating incident flux.

The reaction conversion rate test system utilized a mixing funnel, gate valve, reduced particle bin, N_2 circuit, and macro thermogravimetry (see Fig. 3). Reduced $(Mn_{0.8}Fe_{0.2})_2O_3$ particles were guided out of the particle receiver through the gate valve and dropped into the mixing funnel before being collected in the reduced particle bin under N_2 atmosphere to prevent oxidation. After cooling to ambient temperature, the top layer particles were sent to macro thermogravimetry to obtain the reduction rate during the endothermic process. The reduced particles were heated up to 800 °C at 10 °C/min and held at that temperature until complete oxidization).

The mass curve from macro thermogravimetry was used to calculate the reduction reaction conversion rate, as follows:

$$\alpha_{redu} = \frac{m_{ox,end} - m_{ox,ini}}{m_{ox,end} * \alpha_{redu,max}} \times 100\% \quad (1)$$

Here, $m_{ox,ini}$, $m_{ox,end}$, and $\alpha_{redu,max}$ are the initial particle mass, oxidized particle mass, and maximum weight loss rate, respectively. The maximum weight loss rate is obtained by using simultaneous thermal analyzer. For $(Mn_{0.8}Fe_{0.2})_2O_3$ particles, the maximum reduction conversion rate is 3.36% as reported in Ref. [12].

2.2.3. Flux density distribution measurement setup

A solar simulator system, comprised of 14 xenon lamps, was used to emit concentrated flux onto the controllable-flow particle solar receiver. Each lamp was adjusted to illuminate at its optimal target point. The flux density distribution on a Lambertian target was captured by a CCD-camera, with the grayscale representing the relative flux density of each grid [53]. A flux sensor was placed in a moderate flux density position, which provided a reading. The absolute energy density of each grid on the Lambertian target could be obtained based on the grayscale of the image and the flux density of this point. By taking into consideration the position of the particle receiver, the flux density of the corresponding region could be selected to obtain the distribution on the particle receiver (see Fig. 4).

3. Dynamic model development

3.1. $(Mn_{0.8}Fe_{0.2})_2O_3$ particles reaction kinetics model

The reduction reaction of $(Mn_{0.8}Fe_{0.2})_2O_3$ was shown as Eq. (2) [12]:

$$6(Mn_{0.8}Fe_{0.2})_2O_3 + \Delta H \rightarrow 0.706 \bullet MnFe_2O_4 + 3.294 \cdot Mn_{2.7}Fe_{0.3}O_4 + O_2 \quad (2)$$

Reduction reaction can be quantified by three terms, the extent of conversion term $f(\alpha)$, the temperature term $k(T)$, the pressure term $h(P)$, as Eq. (3) [54].

$$\frac{d\alpha}{dt} = f(\alpha)k(T)h(P) \quad (3)$$

The kinetic models adopt Avrami–Erofeev model.

$$f(\alpha) = 2(1-\alpha)[-\ln(1-\alpha)]^{\frac{1}{2}} \quad (4)$$

The temperature dependence is parameterized through the Arrhenius equation.

$$k(T) = Aexp\left(\frac{-E}{RT}\right) \quad (5)$$

Here, A is the preexponential factor. E is the activation energy.

As the receiver belongs to open system, the pressure term can be regarded as a constant.

$$h(P) = constant \quad (6)$$

3.2. Receiver model

As shown in Fig. 5, the receiver model is divided into five layers [49]. The glass layer serves to transmit the incident flux and reduce convective heat loss. Beneath the glass layer lies the air layer and the particle layer. The particle layer consists of both a flowing particle layer and a stagnant particle layer. The flowing particle layer (with a thickness of approximately 11 mm) is situated atop the receiver and is composed of particles that are actively flowing, whereas the stagnant particle layer consists of those particles blocked by the baffle structure in the lower region. The bottom layer is comprised of a stainless-steel support for thermochemical particle flow, as well as an insulation layer crafted from silica-alumina fiber to provide thermal insulation.

The glass layer, flowing particle layer, stagnant particle layer, and insulation layer were discretized in both time and space using the finite

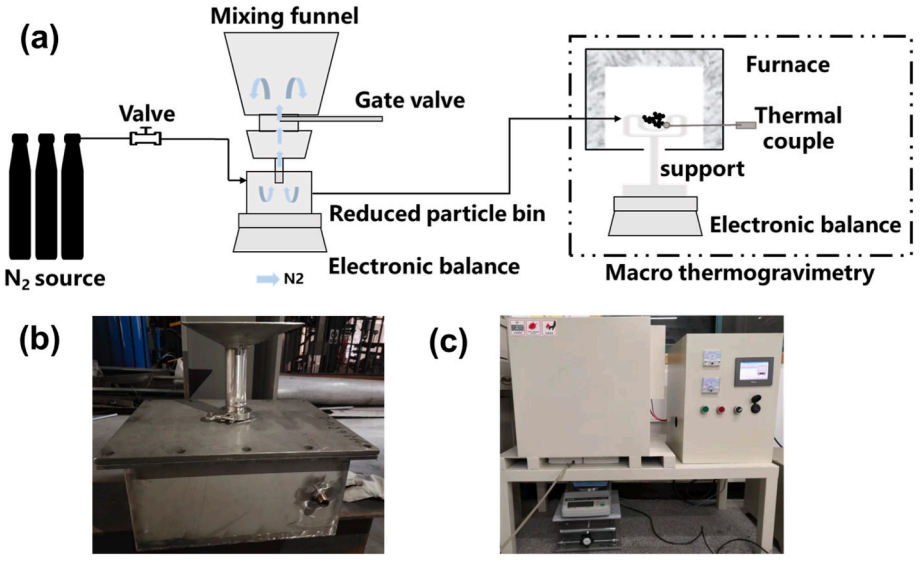

Fig. 3. (a) Schematic diagram of reaction conversion rate test setup. (b) Picture of reduced particle bin. (c) Picture of macro thermogravimetry.

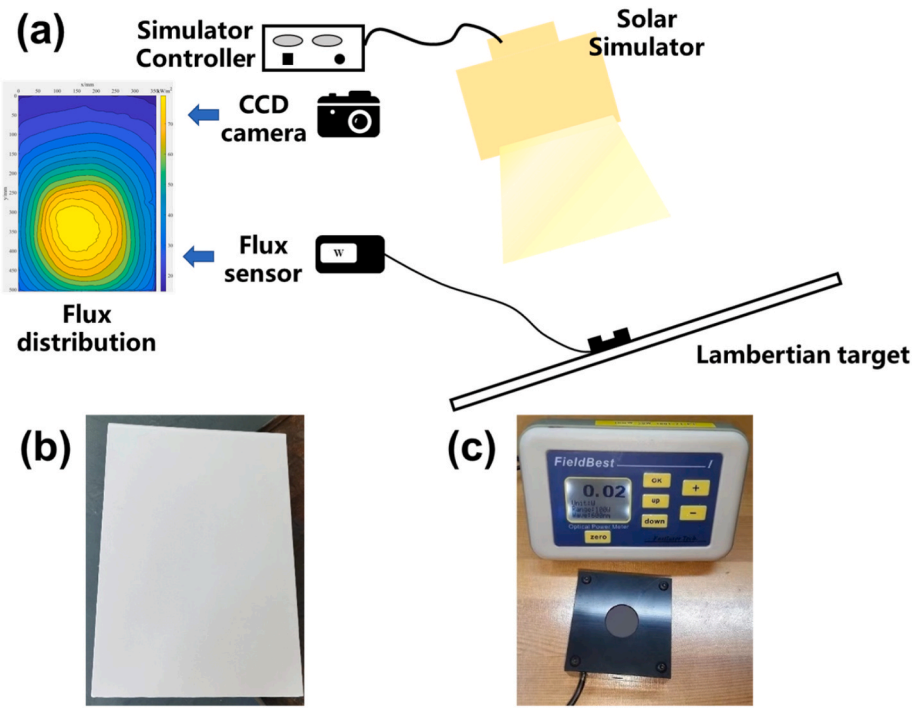

Fig. 4. (a) Schematic diagram of flux density distribution measurement setup. (b) Picture of Lambertian target. (c) picture of flux sensor and meter.

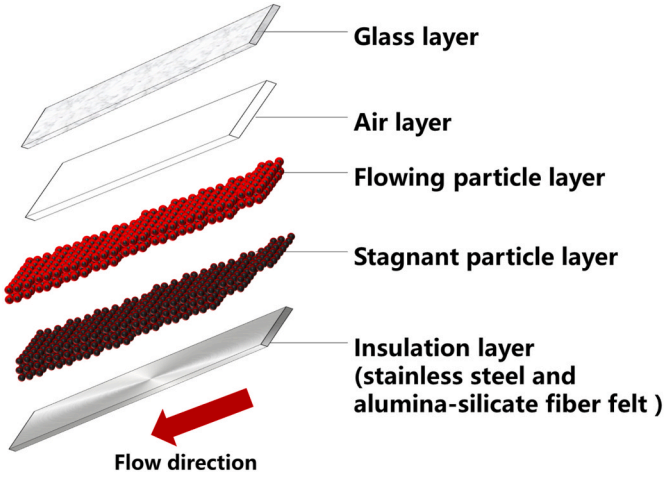

Fig. 5. Schematic diagram of the receiver model structure.

element method, yielding corresponding transient models. Fig. 6(a) presents the primary energy exchange processes between each layer's mesh, as viewed from the vertical cross-section of the particle layer. To further illustrate the energy exchange between the flowing particle layer and its surrounding meshes, Fig. 6(b) showcases the heat conduction and exchange process of the flowing particle layer with its neighboring meshes along a cross-section parallel to the particle layer.

The research primarily focuses on the flowing particle layer, as depicted in Fig. 6(a) and (b). Calculations were conducted for various factors such as incident energy, radiative loss, convective loss, heat conduction from the particles in the surrounding flowing layer, stagnant layer particles, and insulation layer grid. The net influx of heat due to particle flow and thermochemical heat (reaction conversion rate) were also determined, enabling the calculation of the temperature increase of the mesh within this layer.

The incident energy of each grid in the flowing particle layer is as Eq. (7)

$$\dot{Q}_{fp,inc} = I_{rad} \cdot cos\ \theta \cdot \tau_{gla} \cdot \alpha_{fp,rad} \cdot A_{grid} \tag{7}$$

Here, I_{rad} is the incident flux density, θ is the angle between flowing particle layer and the horizontal plane, τ_{gla} is the transmittance of quartz glass, $\alpha_{fp,rad}$ is the absorptivity of $(Mn_{0.8}Fe_{0.2})_2O_3$ particles, A_{grid} is area of each grid.

Radiative loss depends on the particle temperature T_{fp} and the glass temperature T_{gla}, and it is obtained by Eq (8).

$$\dot{Q}_{fp,rad} = -\sigma * \frac{\left[\left(\frac{T_{fp}+273.15}{100}\right)^4 - \left(\frac{T_{gla}+273.15}{100}\right)^4\right]}{X_{fp,gla}} \tag{8}$$

Here, σ is Boltzmann constant, $X_{fp,gla}$ is angle factor from grids of flowing particle layer to glass.

Convective loss is mainly affected by the particle temperature T_{fp} and the glass temperature T_{gla}, the thickness of air layer d_{air}.

$$\dot{Q}_{fp,air} = -\frac{Nu_{air} \cdot \lambda_{air}}{d_{air}} \cdot \left(T_{fp} - T_{gla}\right) \cdot A_{grid} \tag{9}$$

Here, Nu_{air} can be calculated by the empirical formula of Eq. (10) and λ_{air} obtained based on the fitting curve of thermal conductivity of air.

$$Nu_{air} = 0.212 \cdot (GrPr)^{0.25} \tag{10}$$

Conduction loss between grid of flowing particle layer can be calculated as Eq. (11).

$$\dot{Q}_{fp,fp} = -\lambda_{fp} \cdot A_{fp} \cdot \frac{4 * T_{fp} - T_{fp,u} - T_{fp,d} - T_{fp,l} - T_{fp,ri}}{d_{grid}} \tag{11}$$

Here, $T_{fp,u}$, $T_{fp,d}$, $T_{fp,l}$, $T_{fp,r}$ are the temperature of the four adjacent grids in the front, back, left, and right directions, respectively. λ_{fp} is thermal conductivity of particle. A_{fp} is the contact area between adjacent grids of particles in flowing particle layer. d_{grid} is width of grid.

Conduction loss between flowing particle layer and stagnant particle layer depends on the flowing particle temperature T_{fp} and the stagnant

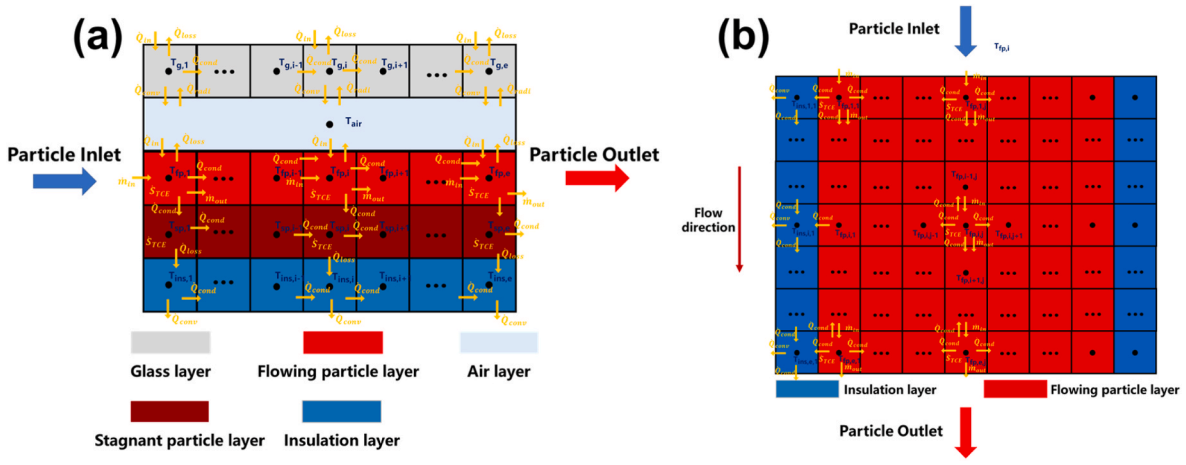

Fig. 6. (a) The structure and energy balance of receiver (vertical cross-section). (b) Heat conduction and exchange of the flowing particle layer (cross-section parallel to the particle layer).

particle temperature T_{sp}, that is defined as Eq. (12).

$$\dot{Q}_{fp,sp} = -\lambda_{fp} \cdot A_{grid} \cdot \frac{T_{fp} - T_{sp}}{\left[\frac{d_{fp} + d_{sp}}{2}\right]} \tag{12}$$

Here, d_{fp} and d_{sp} are thickness of flowing and stagnant particle layer, respectively.

The net influx of heat due to particle flow is calculated as Eq. (13).

$$\dot{Q}_{fp,flow} = \left(h_{s,in} + h_{c,in}\right) \cdot m_{grid,in} - \left(h_{s,out} + h_{c,out}\right) \cdot m_{grid,out} \tag{13}$$

Here, $h_{s,in}$, $h_{c,in}$ and $m_{grid,in}$ are sensible, thermochemical heat and inflow rate of inflowing particles. $m_{grid,out}$ $h_{s,out}$ and $h_{c,out}$ are of outflowing particles. Due to the rectangular shape of the particle channel and its narrow width direction, the flow rate of each grid in the same row perpendicular to the flow direction is considered uniform.

As shown in Eq. (14), thermochemical heat $\dot{Q}_{fp,c}$ is calculated by the reaction conversion rate per unit time $\Delta\dot{\alpha}_{fp,red}$, reaction enthalpy H_{red} and particle mass flow rate m_{grid}.

$$\dot{Q}_{fp,c} = \Delta\dot{\alpha}_{fp,red} \cdot H_{red} \cdot m_{grid} \tag{14}$$

The total heat absorbed is defined as Eq. (15).

$$\dot{Q}_{fp} = \dot{Q}_{fp,inc} + \dot{Q}_{fp,air} + \dot{Q}_{fp,rad} + \dot{Q}_{fp,fp} + \dot{Q}_{fp,sp} + \dot{Q}_{fp,flow} - \dot{Q}_{fp,c} \tag{15}$$

Thus, the temperature increase of flowing particle layer can be calculated as follow:

$$\Delta T_{fp} = \dot{Q}_{fp} \cdot \frac{\Delta t}{C_{fp} \cdot m_{grid}} \tag{16}$$

The particle receiver efficiency $\eta_{receiver}$ can be defined as eq. (16).

$$\eta_{receiver} = \frac{\sum C_{fp,end} \cdot m_{fp,end} \cdot T_{fp,end} + \sum \alpha_{fp,end} \cdot m_{fp,end} \cdot H_{red} - \sum C_{fp,int} \cdot m_{fp,int} \cdot T_{fp,inl}}{\sum I_{rad} \cdot cos\theta \cdot A_{grid}} \tag{17}$$

Here, the first, second and last term of numerator on the RHS is sensible heat of outlet particle, thermochemical heat of outlet particle, sensible heat of inlet particle, respectively. The denominator is total incident flux energy $\dot{Q}_{inc}$.

The glass layer, stagnant particle layer, and insulation layer undergo similar heat transfer processes, which were calculated based on the flowing particle layer for reference.

3.3. Uncertainties analysis

In order to enhance the reliability of the measurement results, uncertainties analysis was conducted to further analyze the errors associated with the measurements. The measurement ranges and uncertainties of different measurement setups are presented in Table 2.

(1) A thermal-electric flux sensor was employed to measure the intensity of concentrated flux at setting measurement point. The flux meter equipped with the sensor has a reading error of ±1%. The total incident energy flux was measured to be 3.55 kW, and its uncertainty was evaluated [53,55]:

$$\delta_{rad} = \sqrt{\delta_{flux}^2 + \delta_{meter}^2} = 0.079\ kW$$

(2) In the particle receiver and reaction conversion rate test setup, K-type armored thermocouples were utilized to measure the temperature of the particles. The temperature data were collected using the Agilent 34972A data logger. Its uncertainty for acquiring the temperature signals from the K-type armored thermocouples is ±0.5 °C. The uncertainty of the particle temperature was evaluated:

$$\delta_T = \sqrt{\delta_{thermocouple}^2 + \delta_{logger}^2} = 2.6\ ^\circ C$$

(3) The DH-10kg electronic scale was employed to measure the outlet particle mass of particle receiver. The uncertainty associated with the measurement data of mass collected by the computer is ±0.02 g. This uncertainty of the particle mass flow rate was evaluated:

$$\delta_M = \sqrt{\delta_{mass}^2 + \delta_{logger}^2} = 0.054\ g/s$$

(4) The JJ1523BC-1520g electronic scale was utilized to measure the changes in particle mass in the reaction conversion rate test setup. The uncertainty associated with the measurement data of mass collected by computer using this scale is ±0.0005 g. This uncertainty was taken into

Table 2
Uncertainties of the different measurement setup.

Measurement Setup	Range	Uncertainty
FB thermal-electric flux sensor for incident flux distribution	0–50 W	±2%
K-type armored thermocouple of particle receiver	0–1300 °C	±2.5 °C
DH-10kg electronic scale for particle flow rate	0–10 kg	±0.05 g
K-type armored thermocouple of reaction conversion rate test setup	0–1300 °C	±2.5 °C
JJ1523BC-1520g electronic scale of reaction conversion rate test setup	0–1520 g	±0.001 g

consideration during the evaluation of the thermochemical reaction conversion rate. The uncertainty of thermochemical reaction conversion rate was evaluated:

$$\delta_\alpha = \sqrt{\delta_\alpha^2 + \delta_{logger}^2} = 0.27\ \%$$

(5) The uncertainty of the particle receiver efficiency was obtained by calculating the uncertainties of the respective parameters involved. When calculating the absorber efficiency, four independent variables were considered: total incident energy flux, particle temperature rise, particle mass flow rate, and thermochemical reaction conversion rate. The uncertainty of particle receiver efficiency was evaluated derived from Eq. (17):

$$\delta_\eta = \sqrt{\left(\frac{\partial \eta}{\partial \dot{Q}_{inc}}\delta_{rad}\right)^2 + \left(\frac{\partial \eta}{\partial T}\delta_T\right)^2 + \left(\frac{\partial \eta}{\partial m_{fp}}\delta_M\right)^2 + \left(\frac{\partial \eta}{\partial \alpha}\delta_\alpha\right)^2} \times 100\%$$

The maximum uncertainty of the particle receiver efficiency is 1.98%.

4. Results and discussions

4.1. Flux density distribution of xenon lamps

As depicted in Fig. 7(a), the flux density distribution produced by the 14 xenon lamps was measured. The resulting energy flux distribution showed a high central energy flux, which gradually decreased towards the edges, closely resembling real concentration profiles. The total incident energy flux, maximum flux density, and average flux density were 3.55 kW, 93.60 kW/m^2, and 78.02 kW/m^2, respectively.

4.2. Validation of $(Mn_{0.8}Fe_{0.2})_2O_3$ particles reaction kinetics model

The mass of $(Mn_{0.8}Fe_{0.2})_2O_3$ particles was measured using a simultaneous thermal analyzer (Hitachi STA7200) with heating rates of 5 °C/min, 10 °C/min, and 20 °C/min to determine the reduction reaction rate. The reaction rate exhibited a trend of slow-fast-slow, with complete reaction occurring in just a few minutes. A reaction kinetics model was employed to calculate the conversion rate for the three heating rates, as illustrated in Fig. 8(a). The accuracy of the simulated results was assessed by comparing experimental data with model data using Root Mean Square Deviation (RMSD) and R-squared (R^2) values. RMSD was employed to quantify the deviation between the simulated and experimental values. A higher RMSD indicates a larger deviation between the two sets of data. The formula used to calculate RMSD is as follows [56].

$$RMSD = \sqrt{\frac{\sum_{i=1}^{n}\left[\left(y_{Exp,i} - y_{Mod,i}\right)\right]^2}{n}} \tag{18}$$

Here, y_{Exp} and y_{Mod} represent the experimental and model calculation results, respectively, while n denotes the number of data sets.

R^2 is used to quantify the degree of fit between the modeling and experimental results, ranging from 0 to 1. A value closer to 1 indicates a better fit. The formula for calculating R^2 is as follows.

$$R^2 = 1 - \frac{\sum_{i=1}^{n}\left[\left(y_{Exp,i} - y_{Mod,i}\right)\right]^2}{\sum_{i=1}^{n}\left[\left(y_{Exp,i} - \bar{y}_{Exp}\right)\right]^2} \tag{19}$$

Herr, $\bar{y}_{Exp}$ represents the average value of the experimental results.

As shown in Fig. 8(b), the calculated results demonstrate that the maximum RMSD is merely 0.0410, and the R^2 values consistently exceed 0.9910. This indicates a high level of agreement between the modeling and experimental data within the reaction temperature range of 1230 K–1330 K.

4.3. Validation of receiver model

To analyze the experimental error in the results, three experiments were conducted under the same conditions of flux density distribution as described in Section 4.1, particle flow rate of 2.1 g/s and so on. Fig. 9(a) – 9(c) present the heating curves and error curves for the three temperature measurement points in different experiments. The three measurement points, P1, P2, and P3, correspond to positions located 10 cm from the outlet, 2 cm from the outlet, and at the outlet, respectively. It can be observed that throughout the entire heating process, the three experiments at the same measurement point exhibit similar heating trends, demonstrating good overall consistency. However, during the initial rapid heating stage (0–1000s), there is some deviation among the experimental data. This deviation can be attributed to the fast-heating rate during the initial rapid heating stage, which results in changes in the particle flow characteristics as the temperature rises. The stable flowing particle layer at room temperature experiences overall sliding during the rapid heating process. This sliding of the particle layer

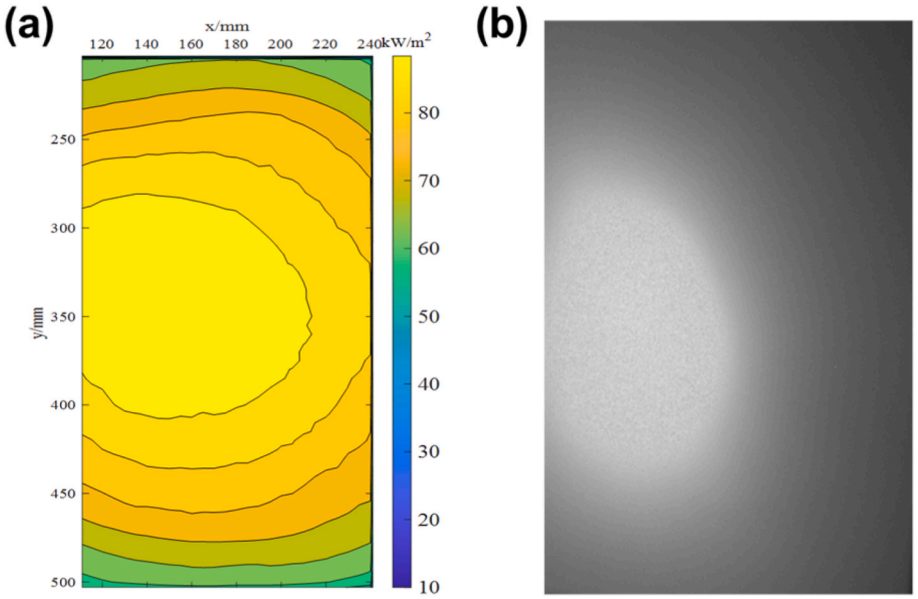

Fig. 7. (a) Flux density distribution on controllable-flow particle solar receiver. (b) Picture of the incident flux emitted from No.3 xenon lamp.

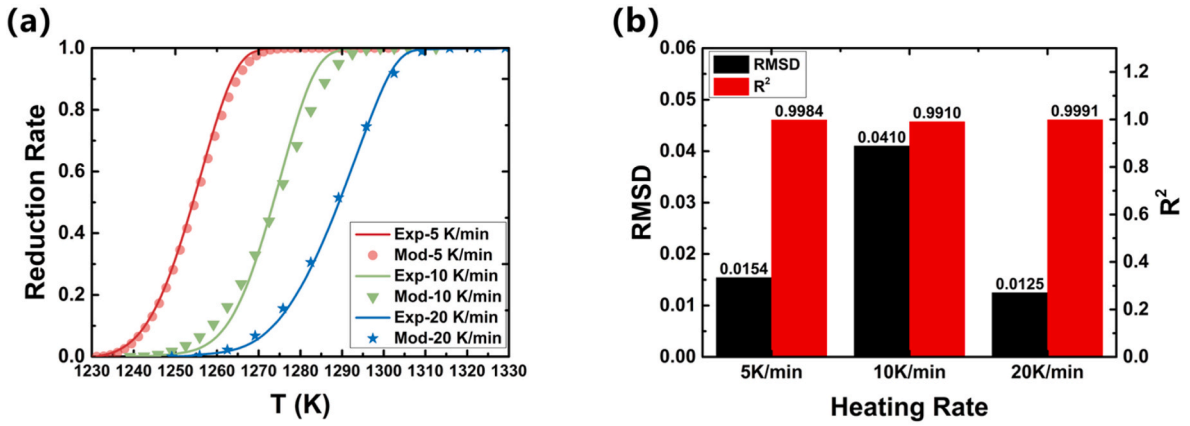

Fig. 8. (a) The reduction reaction rate as a function of T(K) under different heating rates. (b) Deviation of reaction kinetics model compared to TG results.

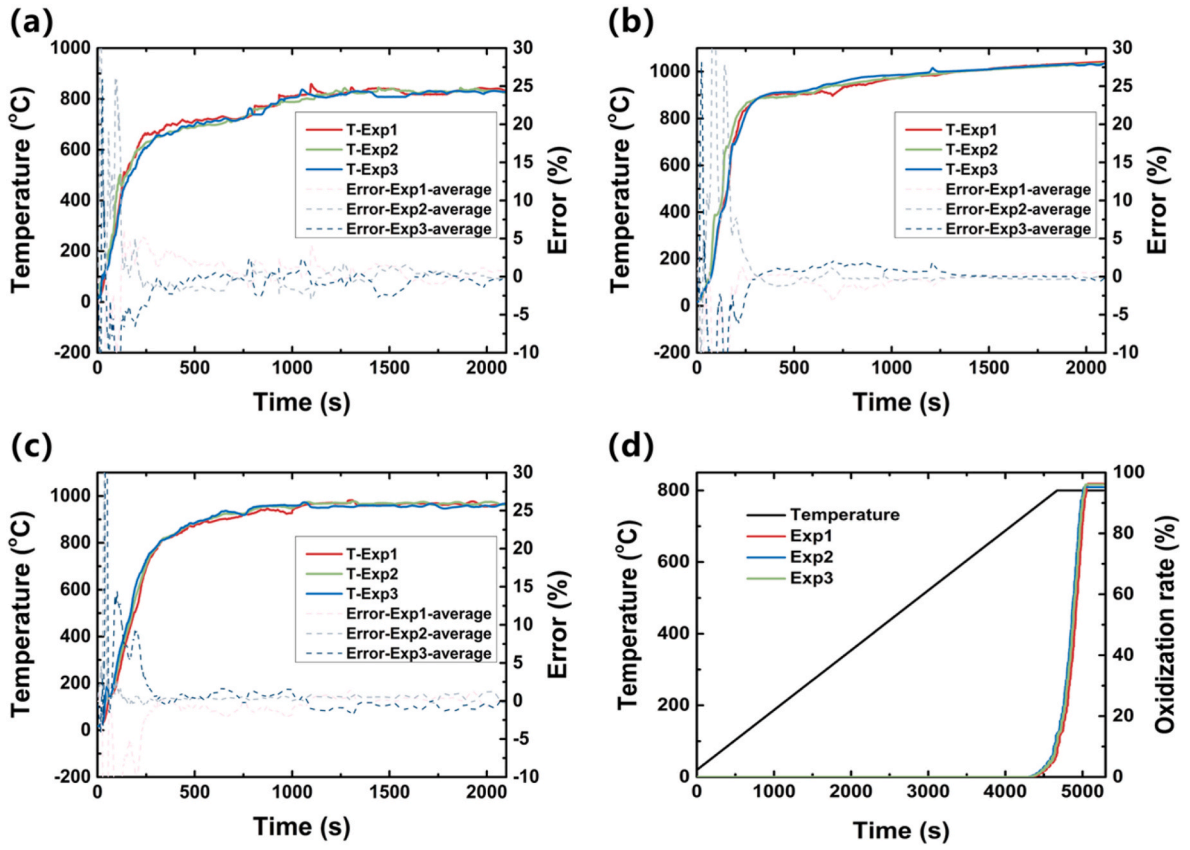

Fig. 9. Repetitive experiments under the same conditions. (a) particle temperature at measurement point P1, (b) particle temperature at measurement point P2, (c) particle temperature at measurement point P3 and (d) outlet particle thermochemical reaction conversion rate at 2100 s.

depends on the initial particle deposition in the flowing particle layer and exhibits a certain degree of randomness. As a result, the heating curves themselves show some fluctuations, as previously discussed [49]. Additionally, during the initial stage with relatively low temperature, small temperature fluctuations can lead to significant deviations among different experiments. These two factors combined result in larger deviations among experiments during the initial stage. Furthermore, the measurement point near the particle inlet, influenced by the connection to the feed buffer tank and the pressure from the high particle accumulation in the tank, exhibits more significant temperature deviations, as shown in Fig. 9(a). As the particle heating rate slows down and the temperature stabilizes, the flow characteristics of the flowing particle layer gradually stabilize as well (1500–2100 s). The temperature deviations among different experiments at the same measurement point gradually decrease and eventually fall within ±2%. At the outlet temperature measurement point, P3, the temperature deviation reaches within ±0.5% (968.5 °C, 962.8 °C, 965.2 °C) at 2100 s. Fig. 9(d) illustrates the macro thermogravimetry results for the particle samples extracted at 2100 s in the three experiments. The corresponding conversion rates are 96.3%, 95.2%, and 96.0%, with errors within 1%. These repetitive experiments demonstrate good repeatability among the different experiments within the same group.

Based on the incident flux density depicted in Fig. 7, a particle flow rate of 2.1 g/s and a total test duration of roughly 2100 s were determined to ensure complete reduction reaction. The experimental and simulated results of three thermocouple measurement points are

presented in Fig. 10(a). The temperature curves exhibited similar heating trends across these three points, with an initial rapid temperature increase, followed by a gradual decrease in heating rate until reaching equilibrium temperature. The experimental temperatures recorded at the three measurement points were 829.5 °C, 1041.8 °C, and 968.5 °C, respectively.

By integrating the receiver model, the heating procedure at these three measurement points was modeled, with simulation outcomes aligning well with experimental results as shown in Fig. 10(b). For the simulated results during the 0–2100 s period, the relatively higher RMSD and lower R^2 values can be attributed to the influence of changes in particle flow characteristics during the rapid heating stage. The flow of the flowing particle layer becomes relatively unstable, leading to temperature fluctuations. The randomness in this flow process results in deviations from the simulated results. Consistent with the previous analysis, this fluctuation is more prominent near the inlet, hence resulting in the highest RMSD and the lowest R^2 values for the P1 measurement point. However, an analysis of the deviations during the relatively stable temperature stage (1500–2100 s) reveals reductions in the deviations for all three temperature measurement points: 11.07 °C, 1.475 °C, and 8.353 °C. This reduction can be attributed to the stabilization of the flowing particle layer as the temperature becomes stable and participation of thermochemical reaction, resulting in smaller temperature fluctuations. As a result, the receiver model achieves better simulation results, with R^2 values exceeding 0.99 in all cases. Furthermore, ongoing experiments and analyses will be conducted to further optimize the receiver model by studying and analyzing the flow of particles during the heating stage. In addition, this study also calculates the receiver efficiency. The simulation based on the receiver model demonstrates that the average outlet temperature of the receiver can reach 1005.9 °C, resulting in a receiver efficiency of 56.9%.

Particle samples were extracted at 1500s, 1800s, and 2100s, and their reaction rates were measured via a macro-thermogravimetric analyzer, as depicted in Fig. 11(a), resulting in values of 53.96%, 87.41%, and 96.35%, respectively.

The average conversion rate of particles at the outlet of the receiver was calculated for these three time points using the receiver model, as presented in Fig. 11(b). The experimental and simulated outcomes demonstrated a significant level of agreement, with errors consistently remaining within the 2% threshold. This close alignment between the observed and simulated results establishes a reliable simulation model, which serves as a robust tool for further analysis of thermochemical reaction processes. Collecting outlet particles within a nitrogen atmosphere and performing real-time measurements of the conversion rate via a macro-thermogravimetric instrument can act as a means to monitor the outlet particle conversion rate, providing crucial parameters and indicators for optimal receiver operation.

4.4. Further research based on the receiver model

4.4.1. Incident flux density

In actual particle receiver operating scenarios, incident flux density may vary due to system scale differences [49]. To investigate the influence of incident flux density on the heat absorption process, this study adjusted the average incident flux density based on the flux distribution of 14 simulated lamps and selected seven different flux densities ranging from 50 kW/m^2 to 1000 kW/m^2 to analyze variations in the exothermic behavior of $(Mn_{0.8}Fe_{0.2})_2O_3$ particles. To ensure complete reaction, the outlet temperature was maintained at ~1010 °C, with the corresponding flow rate being set accordingly. Based on this, changes in outlet particle temperature and reaction conversion rate were simulated during the heating process, as depicted in Fig. 12(a). Using data from these two indicators, the receiver efficiency and reaction time of the main reaction period (conversion rate from 20% to 80%) were compared under different flux densities, as shown in Fig. 12(c).

As radiation intensity increased, receiver efficiency gradually improved, reaching ~88% when radiation intensity reached 1000 kW/m^2. The duration of the fast reaction stage also reduced to ~1 min, which fulfills the requirements for quick and efficient heat absorption. The primary reason for this phenomenon is that although incident flux density increases, the proportion of optical losses in total energy remains relatively stable. However, due to a consistent outlet temperature, the total amount of heat loss under the same heat dissipation area gradually rises, leading to a reduction in the proportion of heat loss in total radiation energy. Consequently, there is an increase in the proportion of energy utilized to consistently heat the particles, leading to a gradual improvement in receiver efficiency from approximately 50%–88% [18]. Moreover, at faster heating rates, the particles spend a longer duration at higher temperatures, which is more conducive to thermochemical reactions. As a result, the duration of the fast reaction stage has reduced from around 13 min to approximately 1 min. This finding indicates that, along with the increase in the average incident flux density, as observed in CSP systems, the enhancement of system scale positively influences the efficiency of the particle receiver and can further contribute to improving the conversion efficiency of solar energy into electricity. This insight highlights the significant advantages associated with scaling up CSP systems. With higher incident flux densities, a larger system size enables a more efficient utilization of thermal energy by the particles, leading to improved performance of the particle receiver.

4.4.2. Reaction enthalpy

As a crucial parameter of thermochemical reaction, an increase in

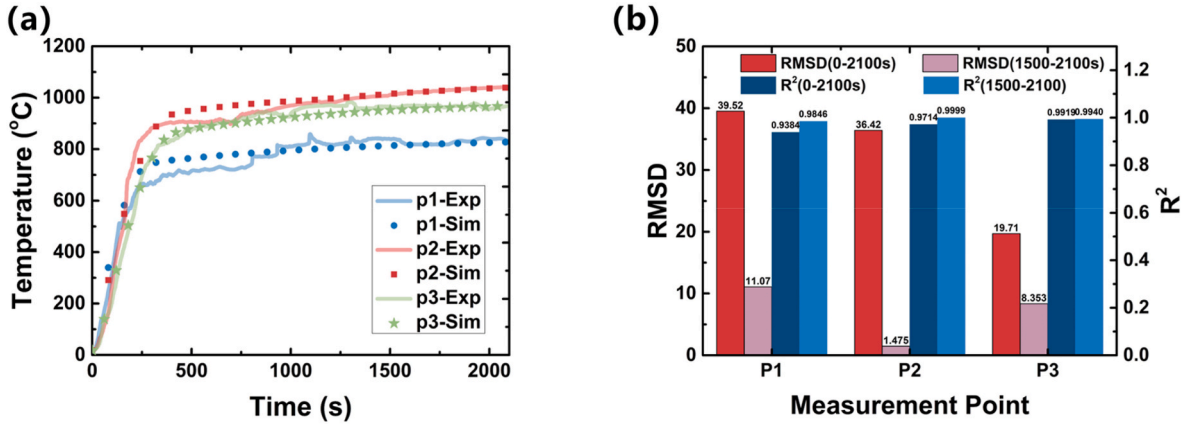

Fig. 10. (a) Experimental and simulated results of temperature increase during the heat absorb process of $(Mn_{0.8}Fe_{0.2})_2O_3$ particles of three thermocouple measurement points. (b) Deviation of receiver model results compared thermocouple measurement.

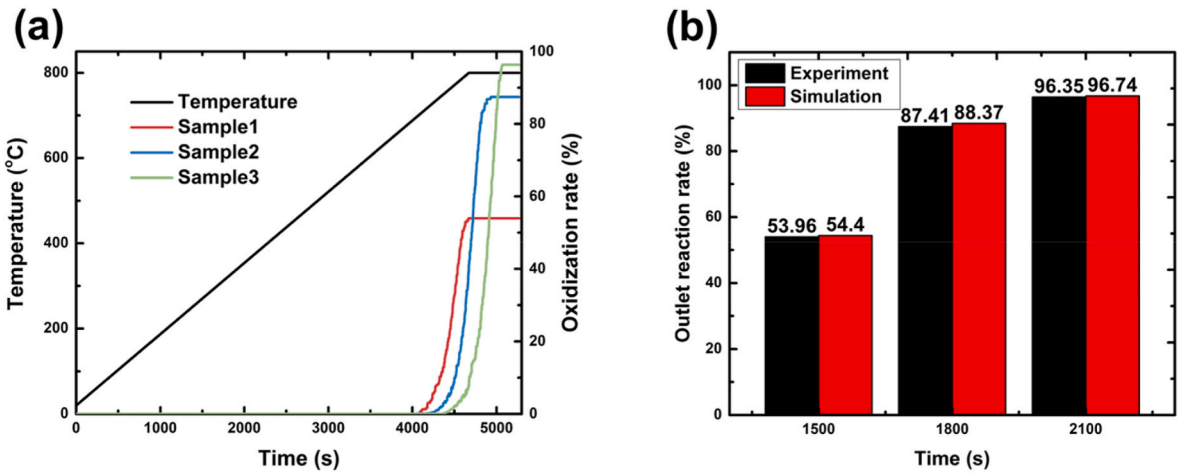

Fig. 11. $(Mn_{0.8}Fe_{0.2})_2O_3$ particles' reaction rates (a) macro thermogravimetry results and (b)comparison of experimental and simulated results.

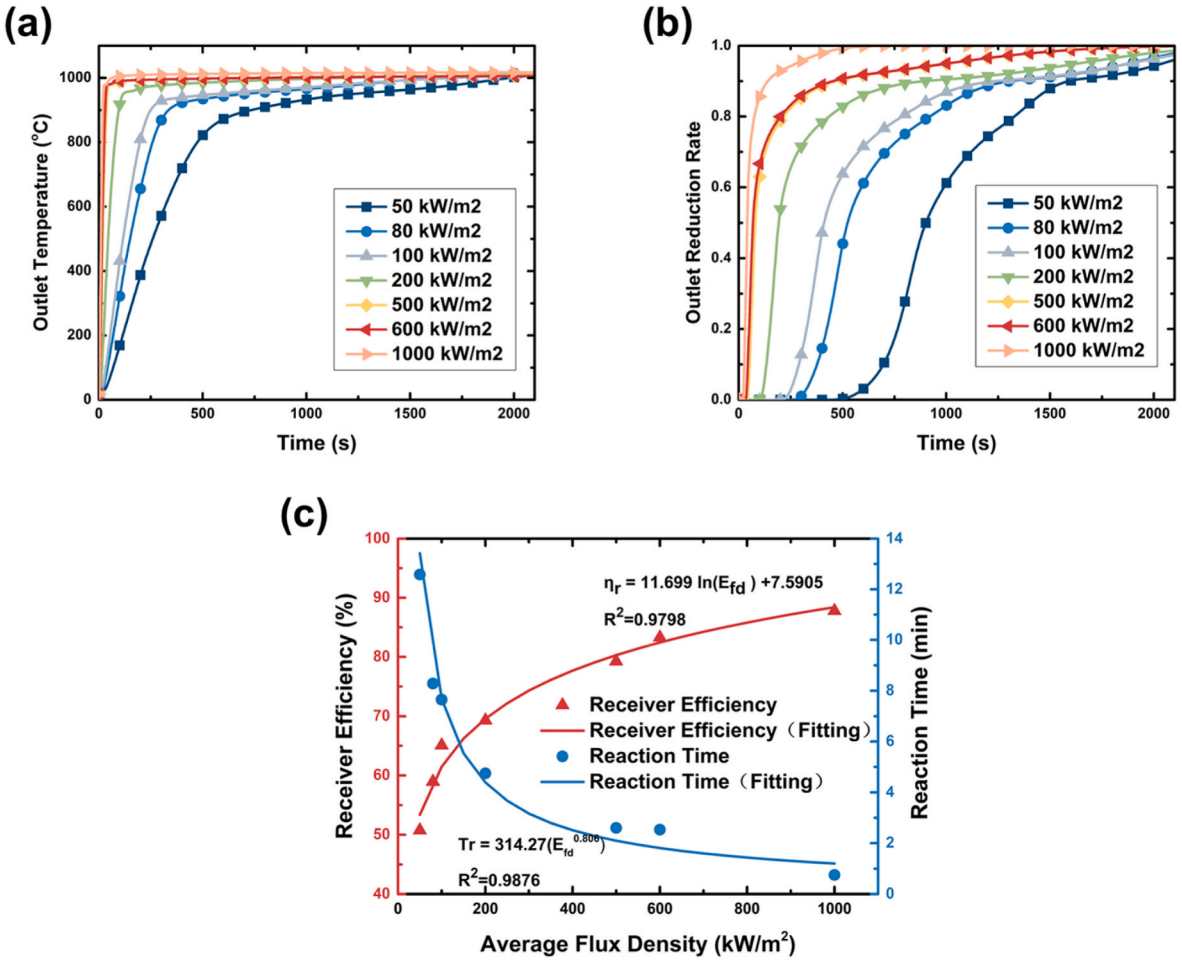

Fig. 12. Simulation results of the particle receiver under different incident flux density. (a) Outlet temperature, (b) outlet reduction rate, (c) receiver efficiency and reaction time (conversion rate from 20% to 80%).

reaction enthalpy can enhance the energy storage density of the medium, thereby reducing the volume of heat absorption and storage equipment and improving system economic efficiency. Therefore, this study analyzed the effect of reaction enthalpy on the exothermic process. Under the same experimental parameters as other conditions, the simulation analyzed the heating process under different reaction enthalpy parameters ranging from 0 kJ/kg to 2000 kJ/kg, with Fig. 13 (a)-(d) presenting changes in outlet temperature, reaction conversion rate, outlet temperature difference, and maximum temperature difference after entering the reaction stage. Under the condition of maintaining a constant reaction rate, with a higher reaction enthalpy, a higher proportion of the incident flux is no longer stored as sensible heat but rather as thermochemical energy. As the temperature enters the reaction temperature zone, the proportion of energy stored as sensible

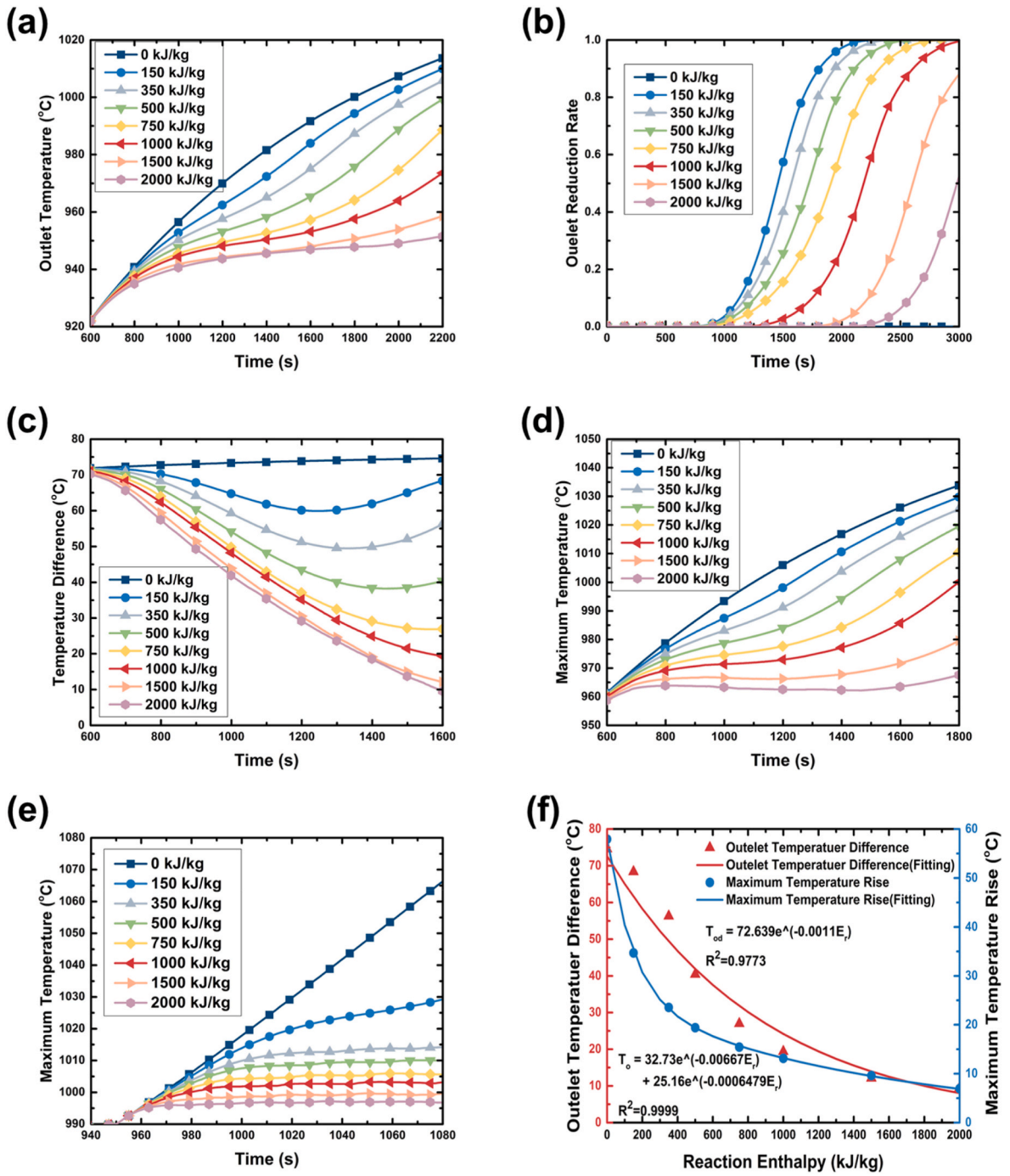

Fig. 13. Simulation results of the particle receiver with different particle reaction enthalpy. (a) Outlet temperature, (b) outlet reduction rate, (c) outlet temperature difference, (d) maximum temperature, (e) maximum temperature under a sudden flux density increase, (e) outlet temperature difference and maximum temperature (under a sudden flux density increase) vs particle reaction enthalpy.

heat decreases. In the main reaction stage (as shown in Fig. 13(a), between 1000 and 2000 s), the proportion of incident flux stored as thermochemical energy increases from 0 (0 kJ/kg) to 83.4% (2000 kJ/kg). Furthermore, the coupling of thermochemical reactions causes the temperature rise rate of the particles to slow down and reach a steady state naturally. Simultaneously, the maximum temperature difference between the outlet particles and the highest temperature of particles in the particle receiver decreases. Both the uniformity of particle temperature distribution at the outlet [57] and the uniformity of temperature distribution on flowing particle layer are improved. The maximum temperature difference of the particles at the outlet section decreases from 74.6 °C (0 kJ/kg) to 9.5 °C (2000 kJ/kg).

Increasing the reaction enthalpy can improve the heat storage capacity per unit temperature rise within the reaction temperature range [58], providing a feasible means to address over-heating triggered by sudden increases in incident solar flux. To simulate a sudden increase in incident flux, the intensity of solar flux was raised by 20% (the average energy flux density increased from 78 kW/m^2 to 94 kW/m^2, and the maximum energy flux density rose from 93 kW/m^2 to 112 kW/m^2) at 950s. Comparing changes in the maximum temperature of the flowing particle layer under different reaction enthalpies, it can be observed from Fig. 13(e) and the blue line in Fig. 13(f) that as reaction enthalpy

rises, the increase of maximum temperature under different enthalpy decreases significantly from 57.89 °C (0 kJ/kg) to only 6.89 °C (2000 kJ/kg), suppressing the temperature spike situation. By enabling spontaneous thermochemical reactions, the temperature spike caused by a sudden increase in incident flux density can be suppressed, providing sufficient buffering time for flow rate regulation and effectively preventing local overheating of the receiver, which supports the stable long-term operation of the particle receiver.

4.4.3. Reaction rate

As another critical parameter of thermochemical reactions, reaction rate also affects the reaction process and particle heat absorption. Different reaction rates lead to changes in the amount of heat stored by particles per unit time when they enter the reaction temperature range and changes in temperature rise rate. To investigate the effect of reaction rate on the exothermic process of thermochemical particles, the heating process of particles was compared under seven different reaction rates ranging from 0.1 × to 10 × based on the $(Mn_{0.8}Fe_{0.2})_2O_3$ reaction rate. By comparing temperature increase curves during the reduction reaction stage, it was observed that as reaction rate increases, both the outlet temperature and the maximum particle temperature decrease. Additionally, the required reaction time shortens from

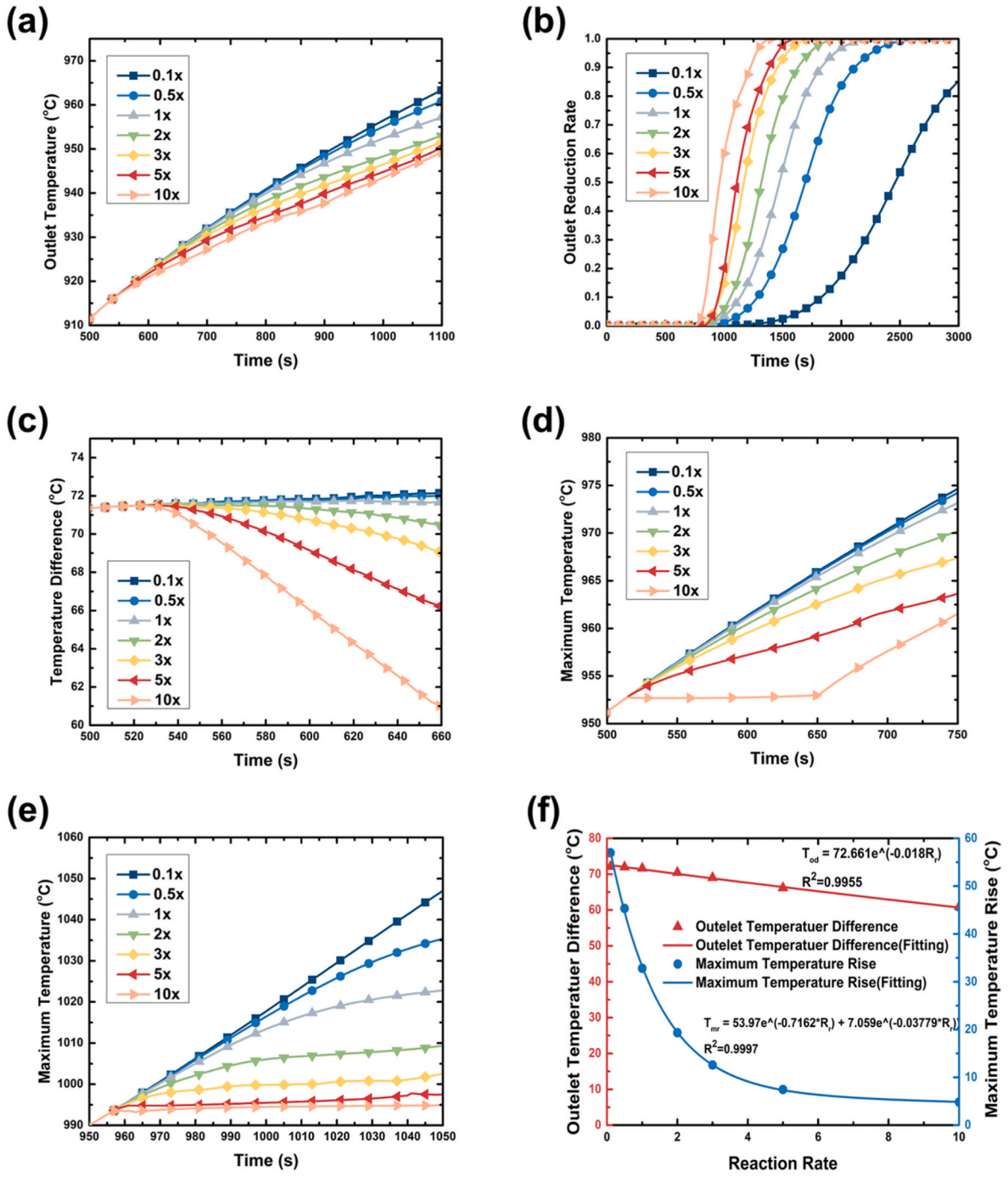

Fig. 14. Simulation results of the particle receiver with different particle reaction rate. (a) Outlet temperature, (b) outlet reduction rate, (c) outlet temperature difference, (d) maximum temperature, (e) maximum temperature under a sudden flux density increase, (e) outlet temperature difference and maximum temperature (under a sudden flux density increase) vs particle reaction rate.

approximately 3500 s (0.1 ×) to about 750 s (10 ×). Similar to the analysis in Section 4.4.2, an elevation in the reaction rate also promotes a higher proportion of the incident flux being stored as thermochemical energy. Consequently, the temperature rise rate of the particles slows down and approaches a steady state naturally. However, it is important to note that at a reaction rate of 10 × , the highest temperature of the flowing particle layer remains relatively constant after entering the reaction temperature range, as depicted in Fig. 14(d). This indicates that a faster reaction rate corresponds to a shorter reaction time. As a result, after the reaction in the high-temperature region concludes, the incident flux continues to be stored as sensible heat, resulting in a continual increase in the highest temperature of the flowing particle layer, as evident from the pink curve in Fig. 14(d). These observations demonstrate that both an increase in reaction enthalpy and reaction rate have a positive effect on improving the uniformity of temperature distribution.

It can be seen that an increase in reaction rate can also enhance the heat storage capacity per unit temperature rise within the reaction temperature range, addressing the issue of over-heating caused by sudden increases in incident flux. When incident flux density is increased by 20% at 950s, changes in the maximum temperature of the flowing particle layer were analyzed. As indicated by Fig. 14(e) and the blue line in Fig. 14(f), an increase in reaction rate resulted in the maximum temperature rise within 130s decreasing from 56.98 °C (0.1 ×) to only 4.84 °C (10 ×), demonstrating that increasing reaction rate can also address the problem of over-heating.

5. Conclusion

This study conducted heat absorption experiments on $(Mn_{0.8}Fe_{0.2})_2O_3$ particles using a controllable-flow particle solar receiver under incident concentrated flux, aiming to achieve a high thermochemical reaction conversion rate and high temperatures under continuous operation. Additionally, a two-dimensional particle receiver model coupled with a reaction kinetics model was established to investigate the heat absorption characteristics of thermochemical particles and the particle receiver. The high-temperature test of $(Mn_{0.8}Fe_{0.2})_2O_3$ particles in the controllable-flow particle solar receiver showed that under the conditions of a total incident flux of 3.55 kW, the temperature of the receiver measurement point could reach 1041.8 °C, the thermochemical reaction conversion rate could reach 96.35%. By coupling with the reaction kinetics model, the simulation results showed that the outlet temperature of the particles could reach 1005.9 °C, and the particle receiver efficiency could reach 56.90%. And an increase in the incident flux density can improve the efficiency of the particle receiver and shorten the reaction time. When the incident flux density reached 1000 kW/m^2, the particle receiver efficiency could reach approximately 88%, and the reaction time could be shortened to around 1 min.

Furthermore, this study investigated the influence of reaction parameters on the temperature uniformity and stability of the heat absorption process. The analysis indicated that both high reaction enthalpy values and reaction rates can improve the uniformity of the outlet particle temperature distribution while reducing the maximum temperature difference at the outlet to 9.53 °C. This approach can mitigate sudden increases in the receiver's maximum temperature by spontaneous thermochemical reactions, allowing for a controlled temperature rise of 6.89 °C (2000 kJ/kg) and 4.84 °C (10 ×). These results demonstrate that thermochemical reactions can enhance the uniformity of temperature distribution and effectively reduce the impact of incident energy flux fluctuations, promoting the long-term stable operation of the particle receiver.

In conclusion, this study conducted an experimental and simulation investigation on the continuous heat absorption of thermochemical storage with high reaction conversion under concentrated flux. It analyzed the dynamic heat absorption process of the particle receiver and examined the impact of key parameters and characteristics on the heat absorption process. The findings reveal the improved temperature distribution uniformity of the particles and the alleviation of overheating issues caused by fluctuating incident flux. These insights contribute to advancing the development of next-generation CSP and TCES technologies, offering promising solutions for renewable energy systems.

Credit author statement

Di Gan: Conceptualization, Methodology, Validation, Software, Writing – original draft, Formal analysis, Writing – review & editing, Visualization. Peiwang Zhu: Discussion, Validation, Formal analysis, Writing – review & editing. Haoran Xu: Validation, Formal analysis, Writing – review & editing. Xiangyu Xie: Investigation, Methodology, Formal analysis. Fengyuan Chai: Investigation, Methodology. Jueyuan Gong: Writing – review & editing. Jiasong Li: Writing – review & editing. Gang Xiao: Funding acquisition, Investigation, Resources, Supervision, Writing – review & editing.

Declaration of competing interest

The authors declare that they have no known competing financial interests or personal relationships that could have appeared to influence the work reported in this paper.

Data availability

Data will be made available on request.

Acknowledgements

The authors gratefully acknowledge the support from the National Natural Science Foundation of China (No. 52176207), Key R&D Program of Zhejiang (NO. 2022C01043) and the Fundamental Research Funds for the Central Universities (2022ZFJH04).

Nomenclature

Latin letters

A	preexponential factor
A	area, m^2
C	Specific heat capacity, J kg^{-1}K^{-1}
d	diameter, m
d	thickness, m
E	activation energy
H	enthalpy, J/kg
I	the incident flux density, kW/m^2
m	mass, kg

P	pressure, Pa
$\dot{Q}$	heat flow rate, W
R	molar gas constant, 8.314J $mol^{-1}K^{-1}$
R^2	correlation coefficient
t	time, s
T	temperature, ^{o}C
X	angle factor

Greek letters

α	absorptivity
α	reaction conversion rate
η	efficiency
θ	angle between flowing particle layer and the horizontal plane
λ	thermal conductivity, W $m^{-1}K^{-1}$
σ	Boltzmann constant
τ	transmittance

Abbreviations

CSP	Concentrating Solar Power
LCOE	Levelized Cost of Electricity
RMSD	Root Mean Square Deviation
TCES	Thermochemical Energy Storage

Subscripts

air	Air layer
c	thermochemical heat
d	adjacent grid below
E	reaction enthalpy
end	end time
fd	flux density
fp	flowing particle layer
flow	particle net flowin
gla	glass layer
grid	grid
in	flow in
inc	incident
ini	initial time
l	adjacent grid on the left
max	maximum
mr	Maximum temperature rise
od	outlet temperature difference
out	flow out
ox	oxidation
s	Sensible heat
sp	Stagnant particle layer
r	receiver
rad	radiation
redu	reduction
ri	adjacent grid on the right
R_r	reaction rate
u	adjacent grid on the upper side Dimensionless groups
Gr	Grashof number
Nu	Nusselt number
Pr	Prandtl number

References

[1] World IRENA. Energy transitions outlook 2023: 1.5°C pathway. Abu dhabi. International Renewable Energy Agency 2023;1:30–2.

[2] Schöniger F, Thonig R, Resch G, Lilliestam J. Making the sun shine at night: comparing the cost of dispatchable concentrating solar power and photovoltaics with storage. Energy Sources B Energy Econ Plann 2021;16(1):55–74. https://doi.org/10.1080/15567249.2020.1843565.

[3] Imran Khan M, Asfand F, Al-Ghamdi SG. Progress in research and technological advancements of commercial concentrated solar thermal power plants. Sol Energy 2023;249:183–226. https://doi.org/10.1016/j.solener.2022.10.041.

[4] Wu S, Zhou C, Doroodchi E, Nellore R, Moghtaderi B. A review on high-temperature thermochemical energy storage based on metal oxides redox cycle. Energy Convers Manag 2018;168:421–53. https://doi.org/10.1016/j.enconman.2018.05.017.

[5] Xu YX, Yan J, Zhao CY. Investigation on application temperature zone and exergy loss regulation based on MgCO3/MgO thermochemical heat storage and release process. Energy 2022;239:122155. https://doi.org/10.1016/j.energy.2021.122155.

[6] Zhang H, Shuai Y, Lougou BG, Jiang B, Yang D, Pan Q, et al. Effects of foam structure on thermochemical characteristics of porous-filled solar reactor. Energy 2022:122219.

[7] Carro A, Chacartegui R, Ortiz C, Becerra JA. Analysis of a thermochemical energy storage system based on the reversible Ca(OH)2/CaO reaction. Energy 2022;261:125064. https://doi.org/10.1016/j.energy.2022.125064.
[8] Han X, Wang L, Ling H, Ge Z, Lin X, Dai X, et al. Critical review of thermochemical energy storage systems based on cobalt, manganese, and copper oxides. Renew Sustain Energy Rev 2022;158:112076. https://doi.org/10.1016/j.rser.2022.112076.
[9] Pardo P, Deydier A, Anxionnaz-Minvielle Z, Rougé S, Cabassud M, Cognet P. A review on high temperature thermochemical heat energy storage. Renew Sustain Energy Rev 2014;32:591–610. https://doi.org/10.1016/j.rser.2013.12.014.
[10] Wong B, Brown L, Schaube F, Tamme R, Sattler C. Oxide based thermochemical heat storage. Conference oxide based thermochemical heat storage. DLR.
[11] Bellan S, Kodama T, Gokon N, Matsubara K. A review on high-temperature thermochemical heat storage: particle reactors and materials based on solid–gas reactions. WIREs Energy and Environment 2022;11(5):e440. https://doi.org/10.1002/wene.440.
[12] Xiang D, Gu C, Xu H, Xiao G. Self-assembled structure evolution of Mn Fe oxides for high temperature thermochemical energy storage. Small 2021;17(29):2101524. https://doi.org/10.1002/smll.202101524.
[13] Wang B, Li L, Pottas JJ, Bader R, Kreider PB, Wheeler VM, et al. Thermal model of a solar thermochemical reactor for metal oxide reduction. J Sol Energy Eng 2020;142(5). https://doi.org/10.1115/1.4046229.
[14] André L, Abanades S, Cassayre L. Appl Sci 2018;8(12):2618. https://doi.org/10.3390/app8122618.
[15] Carrillo AJ, Serrano DP, Pizarro P, Coronado JM. Improving the thermochemical energy storage performance of the Mn2O3/Mn3O4 redox couple by the incorporation of iron. ChemSusChem 2015;8(11):1947–54. https://doi.org/10.1002/cssc.201500148.
[16] Agrafiotis C, Roeb M, Schmuecker M, Sattler C. Exploitation of thermochemical cycles based on solid oxide redox systems for thermochemical storage of solar heat. Part 1: testing of cobalt oxide-based powders. Sol Energy 2014;102(apr):189–211. https://doi.org/10.1016/j.solener.2016.04.034.
[17] Al-Shankiti IA, Ehrhart BD, Ward BJ, Bayon A, Wallace MA, Bader R, et al. Particle design and oxidation kinetics of iron-manganese oxide redox materials for thermochemical energy storage. Sol Energy 2019;183(MAY):17–29. https://doi.org/10.1016/j.solener.2019.02.071.
[18] Carrillo AJ, Chinchilla LE, Iglesias-Juez A, Gutiérrez-Rubio S, Sastre D, Pizarro P, et al. Determining the role of Fe-doping on promoting the thermochemical energy storage performance of (Mn1−xFex)3O4 spinels. Small Methods 2021;5(10):2100550. https://doi.org/10.1002/smtd.202100550.
[19] Wokon M, Block T, Nicolai S, Linder M, Schmücker M. Thermodynamic and kinetic investigation of a technical grade manganese-iron binary oxide for thermochemical energy storage. Sol Energy 2017;153(sep):471–85. https://doi.org/10.1016/j.solener.2017.05.045.
[20] IRENA. Renewable power generation costs in 2021. Abu Dhabi: International Renewable Energy Agency; 2022. p. 121.
[21] Chen X, Zhang Z, Qi C, Ling X, Peng H. State of the art on the high-temperature thermochemical energy storage systems. Energy Convers Manag 2018;177:792–815. https://doi.org/10.1016/j.enconman.2018.10.011.
[22] Flamant G, Grange B, Wheeldon J, Siros F, Valentin B, Bataille F, et al. Opportunities and challenges in using particle circulation loops for concentrated solar power applications. Prog Energy Combust Sci 2023;94:101056. https://doi.org/10.1016/j.pecs.2022.101056.
[23] Yu Y, Bai F, Wang Z. Numerical and experimental investigation on thermal performances of quartz tube gravity-driven solid particle solar receiver based on linear-focused solar furnace. Renew Energy 2023;203:881–97. https://doi.org/10.1016/j.renene.2022.12.126.
[24] Fang W, Chen S, Shi S. Dynamic characteristics and real-time control of a particle-to-sCO2 moving bed heat exchanger assisted by BP neural network. Energy 2022;256:124597. https://doi.org/10.1016/j.energy.2022.124597.
[25] Fang W, Chen S, Xu J, Zeng K. Predicting heat transfer coefficient of a shell-and-plate, moving packed-bed particle-to-sCO2 heat exchanger for concentrating solar power. Energy 2021;217:119389. https://doi.org/10.1016/j.energy.2020.119389.
[26] Tang X-Y, Zhang K-R, Yang W-W, Dou P-Y. Integrated design of solar concentrator and thermochemical reactor guided by optimal solar radiation distribution. Energy 2023;263:125828. https://doi.org/10.1016/j.energy.2022.125828.
[27] Wokon M, Kohzer A, Linder M. Investigations on thermochemical energy storage based on technical grade manganese-iron oxide in a lab-scale packed bed reactor. Sol Energy 2017;153(sep):200–14. https://doi.org/10.1016/j.solener.2017.05.034.
[28] Preisner NC, Bürger I, Wokon M, Linder M. Numerical investigations of a counter-current moving bed reactor for thermochemical energy storage at high temperatures. Energies 2020;13. https://doi.org/10.3390/en13030772.
[29] Mh A, Vmw B, Xiang G, Jp A, Kc A, Awwa D. Reduction of iron–manganese oxide particles in a lab-scale packed-bed reactor for thermochemical energy storage - ScienceDirect. Chem Eng Sci.221. https://doi.org/10.1016/j.ces.2020.115700.
[30] Bo W, Wheeler VM, Pottas J, Kreider PB, Lipinski W. Thermal modelling of a solar thermochemical reactor for metal oxide reduction. International Heat Transfer Conference 162018. p. 7443-7449.
[31] Bo WA, Ll A, Fs B, Jjp A, Ak A, Vmw C, et al. Thermal reduction of iron–manganese oxide particles in a high-temperature packed-bed solar thermochemical reactor. Chem Eng J.412. https://doi.org/10.1016/j.cej.2020.128255.
[32] Tescari S, Neumann NC, Sundarraj P, Moumin G, Duarte J, Linder M, et al. Storing solar energy in continuously moving redox particles – experimental analysis of charging and discharging reactors. Appl Energy 2022;308:118271. https://doi.org/10.1016/j.apenergy.2021.118271.
[33] Schrader AJ, Schieber GL, Ambrosini A, Loutzenhiser PG. Experimental demonstration of a 5kWth granular-flow reactor for solar thermochemical energy storage with aluminum-doped calcium manganite particles. Appl Therm Eng 2020;173:115257. https://doi.org/10.1016/j.applthermaleng.2020.115257.
[34] Zhou X, Mahmood M, Chen J, Yang T, Xiao G, Ferrari ML. Validated model of thermochemical energy storage based on cobalt oxides. Appl Therm Eng 2019;159:113965. https://doi.org/10.1016/j.applthermaleng.2019.113965.
[35] Huang W, Korba D, Randhir K, Petrasch J, Klausner J, Auyeung N, et al. Thermochemical reduction modeling in a high-temperature moving-bed reactor for energy storage: 1D model. Appl Energy 2022;306:118009. https://doi.org/10.1016/j.apenergy.2021.118009.
[36] Korba D, Huang W, Randhir K, Petrasch J, Klausner J, AuYeung N, et al. A continuum model for heat and mass transfer in moving-bed reactors for thermochemical energy storage. Appl Energy 2022;313:118842. https://doi.org/10.1016/j.apenergy.2022.118842.
[37] Nie F, Bai F, Wang Z, Li X, Yang R. Solid particle solar receivers in the next-generation concentrated solar power plant. EcoMat 2022;4(5):e12207. https://doi.org/10.1002/eom2.12207.
[38] Jiang K, Du X, Kong Y, Xu C, Ju X. A comprehensive review on solid particle receivers of concentrated solar power. Renew Sustain Energy Rev 2019;116:109463. https://doi.org/10.1016/j.rser.2019.109463.
[39] Ho CK. Advances in central receivers for concentrating solar applications. Sol Energy 2017;152(aug):38–56. https://doi.org/10.1016/j.solener.2017.03.048.
[40] Rovense F, Reyes-Belmonte MÁ, Romero M, González-Aguilar J. Thermo-economic analysis of a particle-based multi-tower solar power plant using unfired combined cycle for evening peak power generation. Energy 2022;240:122798. https://doi.org/10.1016/j.energy.2021.122798.
[41] Mills BH, Ho CK, Schroeder NR, Shaeffer R, Laubscher HF, Albrecht KJ. Design evaluation of a next-generation high-temperature particle receiver for concentrating solar thermal applications. Energies 2022;15. https://doi.org/10.3390/en15051657.
[42] González-Portillo L, Albrecht K, Ho CK. Techno-economic optimization of CSP plants with free-falling particle receivers. Entropy 2021;(1). https://doi.org/10.3390/e23010076.
[43] Ho CK, Christian JM, Yellowhair J, Armijo K, Nguyen C. Performance evaluation of a high-temperature falling particle receiver. Technology, American Society of Mechanical Engineers; 2016. V001T004A006–V001T004A006.
[44] Frantz C, Buck R, Amsbeck L. Design and cost study of improved scaled-up centrifugal particle receiver based on simulation. In Proceedings of the ASME 2020 14th International Conference on Energy Sustainability, Virtual Online Conference; 17–18 June 2020. V001T002A005.
[45] Moumin G, Tescari S, Sundarraj P, de Oliveira L, Roeb M, Sattler C. Solar treatment of cohesive particles in a directly irradiated rotary kiln. Sol Energy 2019. https://doi.org/10.1016/j.solener.2019.01.093.
[46] Jiang K, Tian Z, Chen S, Xu C, Du X. Numerical simulation on gas-solid flow characteristics in a high-density countercurrent fluidized bed particle solar receiver. Sol Energy 2023. https://doi.org/10.1016/j.solener.2022.11.048.
[47] Kang Q, Flamant G, Dewil R, Baeyens J, Zhang H, Deng YM. Particles in a circulation loop for solar energy capture and storage. Particuology 2019. https://doi.org/10.1016/j.partic.2018.01.009.
[48] Nie F, Yu Y-Y, Bai F, Wang Z. Experimental and numerical investigation on thermal performance of a quartz tube solid particle solar receiver. Sol Energy 2020;207:1055–69. https://doi.org/10.1016/j.solener.2020.07.013.
[49] Xie X, Xu H, Gan D, Ni M-j, Yan J-h, Cen K, et al. A sliding-bed particle solar receiver with controlling particle flow velocity for high-temperature thermal power generation. Renew Energy 2021. https://doi.org/10.1016/j.renene.2021.10.083.
[50] Xie X, Xiao G, Ni M, Yan J, Cen K. Optical and thermal performance of a novel solar particle receiver. Conference Optical and thermal performance of a novel solar particle receiver. American Institute of Physics Inc.
[51] Carrillo AJ, Moya J, Bayón A, Jana P, de la Peña O'Shea VA, Romero M, et al. Thermochemical energy storage at high temperature via redox cycles of Mn and Co oxides: pure oxides versus mixed ones. Sol Energy Mater Sol Cell 2014;123:47–57. https://doi.org/10.1016/j.solmat.2013.12.018.
[52] Gan D, Sheng H, Zhu P, Xu H, Xiao G. Long-term replenishment strategy of SiC-doped Mn-Fe particles for high-temperature thermochemical energy storage. Sol Energy 2023;262:111842. https://doi.org/10.1016/j.solener.2023.111842.
[53] Xiao G, Guo K, Xu W, Ni M-j, Luo Z-y, Cen K. An improved method of Lambertian CCD-camera radiation flux measurement based on SMARTS (simple model of the atmospheric radiative transfer of sunshine) to reduce spectral errors. Energy 2014;67:74–80. https://doi.org/10.1016/j.energy.2013.12.055.
[54] Vyazovkin S, Burnham AK, Criado JM, Pérez-Maqueda LA, Popescu C, Sbirrazzuoli N. ICTAC Kinetics Committee recommendations for performing kinetic computations on thermal analysis data. Thermochim Acta 2011;520:1–19. https://doi.org/10.1016/j.tca.2011.03.034.
[55] Liu L, Zhang Q, Zou S, Du S, Meng F. Experimental study on dynamic thermal characteristics of novel thermosyphon with latent thermal energy storage condenser. Energy 2023;282:128196. https://doi.org/10.1016/j.energy.2023.128196.

[56] Hu T, Kwan TH, Zhang H, Wang Q, Pei G. Thermal performance investigation of the newly shaped vacuum tubes of parabolic trough collector system. Energy 2023; 278:127802. https://doi.org/10.1016/j.energy.2023.127802.
[57] Yu M-f, Mi X-l, Zhang X-M, Yang Z-s, Huang Q, Zhou K, et al. Numerical study of free-falling particle receivers with curtain and particle interchange for high receiver efficiency and low temperature difference. Sol Energy 2022. https://doi.org/10.1016/j.solener.2022.07.025.
[58] Yuan P, Gu C-d, Xu H, Ning Z, Cen K, Xiao G. Regulating thermochemical redox temperature via oxygen defect engineering for protection of solar molten salt receivers. iScience 2021;24. https://doi.org/10.1016/j.isci.2021.103039.